# SIP: Simultaneous Isotope Production Via Deuteron Break-up

E.F. Matthews[a,*], J. Corvino[a,c], E. K. Still[a,b], I. C. Meyer[a], E. Y. Maas[a,c]

[a]*Department of Nuclear Engineering, University of California, Berkeley, California 94720*
[b]*Department of Materials Science and Engineering, University of California, Berkeley, California 94720*
[c]*Department of Chemical Engineering, University of California, Berkeley, California 94720*

## Abstract

A design for the simultaneous production of various medical isotopes using a single accelerator beam has been developed. A beam of deuterons impinges on a series of three foils. The first foil produces a radioisotope via a $(D, x)$ reaction, the second breaks up the transmitted deuteron beam, the third uses the high energy break-up neutrons to produce a second radioisotope via a $(n, x)$ reaction. A preliminary model of the experiment was developed in MCNP to predict the spectra of key particles at specific points of the design. A set of four candidate materials were investigated through mechanical analysis and radiation studies for use in the deuteron breakup target. The mechanical analysis led to the design of a stage and foil system, using SOLIDWORKS®, that minimizes likelihood of plastic deformation and subsequent failure. The risks with regards to heat transfer occurring in the system were explored using simulations preformed in COMSOL Multiphysics®. A chemical separation technique using dual ion exchange columns was devised based upon previous research. This allows for a quick, inexpensive, and high-purity separation of Cu-64,67 and Y-88. A experimental test of this concept was performed and analyzed; three medically relevant radioisotopes were produced: $^{90}\text{Zr}(D, \alpha)^{88}\text{Y}$, $^{64}\text{Zn}(n, p)^{64}\text{Cu}$, and $^{67}\text{Zn}(n, p)^{67}\text{Cu}$.

*Keywords:* medical isotopes, deuteron break-up, charged particle reactions

## 1. Motivation

Historically, medically important radionuclides have been produced by two major means: nuclear reactors and proton accelerators [1]. The latter has largely been conducted using small hospital cyclotrons and two major production facilities at Los Alamos and Brookhaven National Laboratories [1]. While these proton beam capabilities have proven useful, they are inherently wasteful. After passing a through enough material, the proton beam will lose energy and cease to contribute to the radioisotope yield. It has been proposed that this issue can be addressed by introducing deuteron break-up. If deuterons are accelerated rather than protons, a deuteron break-up target could be introduced produce neutrons for an additional

---

*Corresponding author
*Email address:* efmatthews@berkeley.edu (E.F. Matthews)

set of radioisotope production. In this study, this idea is explored both experimentally and theoretically in design-space.

An experimental beam stack was designed and run with 30 MeV and 50 MeV deuterons to measure the yield of medically useful radioisotopes. The experiment was performed at the 88 inch cyclotron at Lawrence Berkeley National Laboratory from February 10 to 13, 2017. In this experiment, three reactions of medical interest were observed: $^{90}$Zr$(D, \alpha)^{88}$Y in a zirconium foil exposed to a deuteron beam and $^{64}$Zn$(n, p)^{64}$Cu and $^{67}$Zn$(n, p)^{67}$Cu in a zinc foil exposed to a break-up neutrons from that same deuteron beam. $^{88}$Y is a long-lived (106.6 d [2]) radioisotope with strong Auger electron emission that has been proposed as a long-term therapeutic cancer treatment [3]. $^{64}$Cu and $^{67}$Cu form a "theranostic" pair, meaning that when used in conjunction both diagnostic imaging and therapeutic treatment can be simultaneously obtained [1].

The following offers an outline of the considerations that were taken in the analysis of the experiment and design of an optimized simultaneous radioisotope production beam stack. The data from the experiment is analyzed and the result are presented. This offers a proof-of-concept and offers vital data to tailor future beam stacks. In the design of a new stack, it would be helpful to have estimates for the production of the isotopes based on changing various parameters, such as foil thicknesses. This will be achieved through a Monte-Carlo radiation transport simulation of the design in the Monte-Carlo n-Particle code (MCNP) with proposed work for a more adaptable simulation. A materials selection matrix was compiled to optimize the material properties of the deuteron break up target such that premature failure is avoided and a high neutron flux is achieved. The heat transfer due to irradiation was modeled in order to determine the range of safe operating conditions. After irradiation, the metal foils will contain mainly zinc and zirconium with trace amounts of copper and yttrium, respectively. In order for the copper and yttrium to be used as medical isotopes, they must be separated and purified (> 98% pure), thus a chemical separation method is required for this design.

## 2. Experimental Benchmark and Production Model - Eric Matthews

### 2.1. Experiment and Procedure

An experiment to benchmark the efficacy of the concept of simultaneous radioisotope production was performed from February 10 to 13, 2017. Two foil stacks were assembled and each was run with a 30 MeV and 50 MeV deuteron beam, respectively. In the front series of foil, the medically relevant reaction $^{90}$Zr$(D, \alpha)^{88}$Y was observed. The deuterons transmitted through the front foil stack were then incident on a beryllium target. Within this target some portion of the deuterons underwent excitation by the Coulomb field of the target nuclei. As the deuteron nucleus is weakly bound some of these excited nuclei break up into a separate proton and neutron. The protons that are generated in the break-up have charge and thus have a finite range in matter and will stop in the beryllium target. The break-up neutrons have no charge and thus continue through the break-up foil.

Figures 1 and 2 show foil stack designs for the each of the 50 MeV and 30 MeV deuteron runs, respectively. In each, it can be seen there are a series of iron, zirconium, and titanium

foils. In order to maximize the use of the beam time, these additional foils were put in place to measure energy-dependent deuteron reaction cross sections. These additional measurements were not related to this work and will not be discussed. The yield of $^{88}$Y from $(D, \alpha)$ on $^{90}$Zr was measured from the front zirconium foil only. A series of aluminum degraders were put in place to lower the deuteron beam energy between each set of foils for the purposes of the ride-along energy-dependent cross section measurements. The deuterons that were transmitted through these front foils then impinge on the beryllium target creating break-up neutrons. The beryllium target used in the experiment was not as thick as the range of the deuterons that impinged on it, therefore, an aluminum stopper was placed after the beryllium break-up target to ensure no deuterons reacted with the subsequent zinc foils. The break-up neutrons continue on through the beryllium target and aluminum stopper and undergo nuclear reactions in the zinc foil. The yields of $^{64}$Cu and $^{67}$Cu from $(n, p)$ on natural zinc were measured. Each beam stack was irradiated with a beam current of 100 nA for 20 minutes.
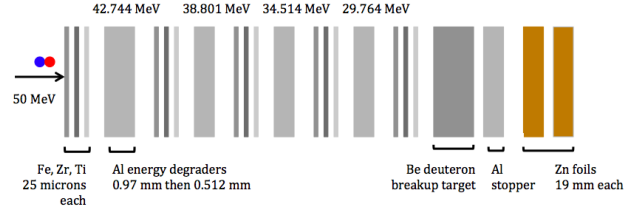


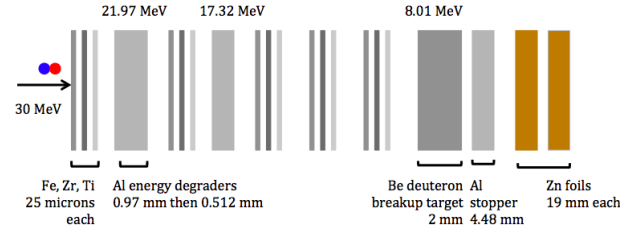Figure 1: Foil stack design for 50 MeV deuteron experiment.



Figure 2: Foil stack design for 30 MeV deuteron experiment.

After each irradiation the foils were moved to the counting lab. A high purity germanium detector (HPGe) was used to observe the gamma-ray emissions from each foil. HPGe's were used as they have superior photon energy resolution and thus allow for precision measurements. When a gamma ray interacts in within the detector volume, it deposits some portion of its energy. The energy deposited creates an electronic signal that can be read out from electrodes on the detector. The magnitude of the signal is directly proportional the energy deposited that created the signal. An analog-to-digital converter (ADC) can be used to histogram the various signals created over the observation time by magnitude. This histogram yields the gamma-ray spectrum of the sample being counted. The efficiency of the detector as a function of incident photon energy can be assessed using a source with a

3

well characterized activity. In this experiment a $^{152}$Eu calibration source was used to ascertain the efficiency of the detector. $^{152}$Eu is an ideal calibration source as its gamma-ray spectrum is well characterized and it emits several gamma-rays spanning the 100-1400 keV photon energy region. Equation 1 details the logarithmic polynomial functional form to which the efficiency data was fit. This functional form features a region of low efficiency for low-energy photons which occurs due to high attenuation of these photons through the housing of the detector. The model has a peak in efficiency around 50 keV and then the detection decreases with increasing photon energy, much like that of the photoelectric cross section of germanium. Figure 3 shows the fit that was obtained.

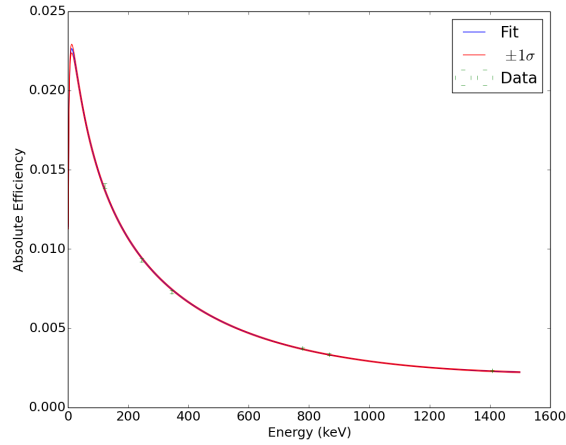$$\varepsilon = B_0 ln(E_\gamma)^3 + B_1 ln(E_\gamma)^2 + B_2 ln(E_\gamma) \tag{1}$$



Figure 3: Efficiency calibration of the HPGe used in this experiment. The measured gamma emissions from the $^{152}$Eu source were fit to the functional form detailed in Eq. 1.

As previously stated, the electronic response of the HPGe detector is highly linear and can be fit with a linear form as shown in Eq. 2. Figure 4 displays the fit that was obtained. Both the energy and efficiency calibrations were obtained using the NumPy regression library for the Python programming language [4].
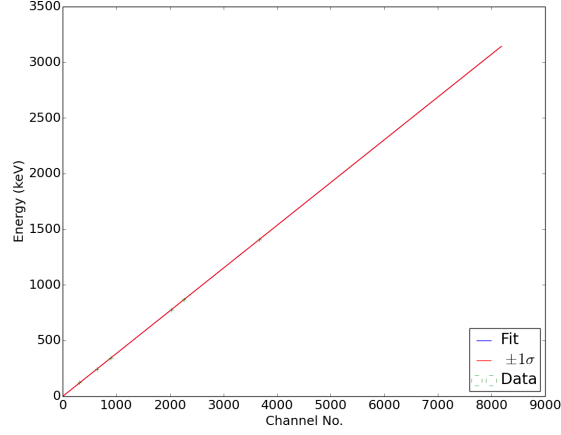
$$\varepsilon = B_0 + B_1 E_\gamma \tag{2}$$

4

Figure 4: Energy calibration of the HPGe used in this experiment. The measured gamma emissions from the $^{152}$Eu source were fit to a line as given by Eq. 2.

## 2.2. Data Analysis and Results

Figures 5a and 6a show the gamma-ray spectra collected from the front zirconium foil of the 30 MeV and 50 MeV deuteron runs, respectively. $^{88}$Y emits a discrete-energy 1836.1 keV gamma ray [2]. Each of the spectra were thus zoomed into this energy region in Figs. 5b and 6b to look for emissions of this gamma-ray.

As can be seen in Fig. 5b, the 30 MeV deuteron run data did not show a 1836.1 keV photopeak that was detectable above the Compton background of the HPGe. This does not mean that $^{88}$Y was not produced. The count time for this spectrum was relatively short in comparison the half-life of $^{88}$Y, therefore, the photopeak may have been detected had the counting duration been longer. $^{88}$Y has a half-life of 106.6 days [2], so as of May 11, 2017, further counting of the front foil is still possible as only approximately one half-life of the $^{88}$Y has elapsed. This data could be obtained and analyzed in future work. As can be seen in Fig. 6b, the 50 MeV deuteron run data did indeed show a 1836.1 keV photopeak observable over background.

Figures 7a and 7b show the gamma-ray spectra collected from the natural zinc foils of the 30 MeV and 50 MeV deuterons runs. $^{67}$Cu has a strong gamma emission with a discrete energy of 184.6 keV [2]. The radioisotope $^{64}$Cu does not have a strong, discrete gamma emission, however, it is a positron emitter [2]. The positron is the anti-particle of the electron. When a positron and electron collide they annihilate, resulting in the emission of two 511 keV photons. The positrons emitted from the $^{64}$Cu sample, quickly slow and annihilate with the electrons of neighboring atoms. Thus $^{64}$Cu is a strong emitter of 511 keV annihilation photons. Both Figs. 7a and 7b exhibit a photopeak at 184.6 keV and 511 keV, indicating $^{67}$Cu and $^{64}$Cu were produced.
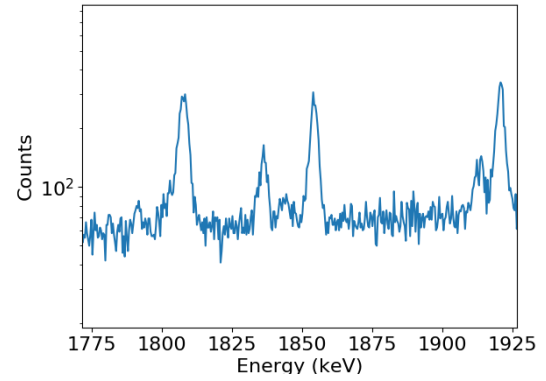
5
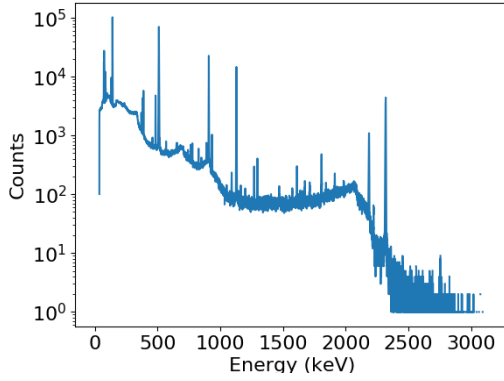
(a) Gamma-ray spectrum of front zirconium foil from 30 MeV deuteron run. The detector count time was 1881 seconds with a live time ratio of 0.957.
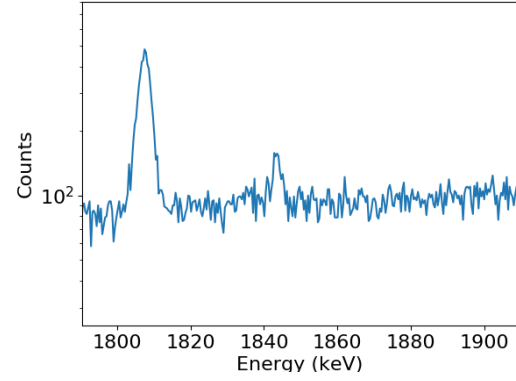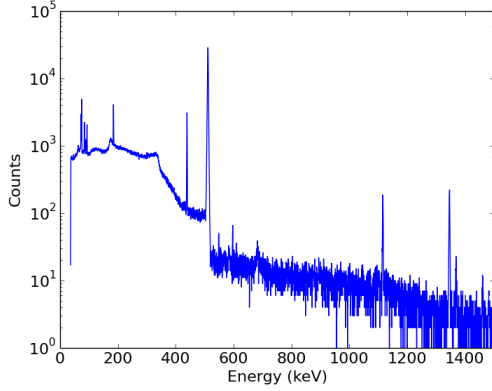


(b) Zoomed to energy region of interest.
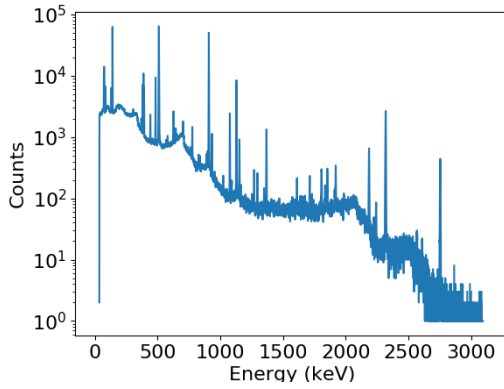


(a) Gamma-ray spectrum of front zirconium foil from 50 MeV deuteron run. The detector count time was 1597 seconds with a live time ratio of 0.951.



(b) Zoomed to energy region of interest.

(a) Gamma-ray spectrum of zinc foils exposed to break-up neutrons from 30 MeV deuteron run. The detector count time was 21600 seconds with a live time ratio of 0.9993.
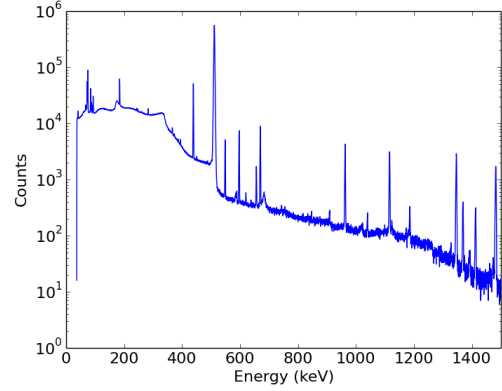
(b) Gamma-ray spectrum of zinc foils exposed to break-up neutrons from 50 MeV deuteron run. The detector count time was 21600 seconds with a live time ratio of 0.9850.

When a radioisotope is produced, its population grows with the reaction rate that produces it, $R$, and decays by its own activity, $A$. This simulanteous growth and decay gives the net rate of change as a function of time in the population, $N$, of the radioisotope and is described by the following differential equation:

$$\frac{\partial N}{\partial t} = R - A \tag{3}$$

The activity of a radioisotope is the product of its time-dependent population, $N(t)$, and its decay constant $\lambda$. Therefore, Eq. 3 becomes:

$$\frac{\partial N}{\partial t} = R - \lambda N(t) \tag{4}$$

Solving this differential equation and applying the initial condition that there is no radioisotope present at the start of time ($N(0) = 0$) yields the solution:

$$N(t) = \frac{R}{\lambda}(1 - e^{-\lambda t}) \tag{5}$$

And thus the activity is:

$$A(t) = \lambda N(t) = R(1 - e^{-\lambda t}) \tag{6}$$

Similarly, if the initial condition is rather that there is some activity of radioisotope initially present ($A(0) = A_0$) but there is no external production of the radioisotope ($R = 0$), then the simple exponential decay law is found:

$$A(t) = A_0 e^{-\lambda t} \tag{7}$$

If a decaying sample is observed by a detector over a period of time, $t_1$ to $t_2$, the number of counts the detector will observe, $C$, is given by the integral of the activity weighted by the

7

detector efficiency for that gamma energy, $\varepsilon(E_\gamma)$, the gamma intensity, $I_\gamma$, and the detector live time ratio, $L$:

$$C = \varepsilon(E_\gamma) I_\gamma L \int_{t_1}^{t_2} A(t)\, dt \tag{8}$$

where $t_1$ is the time between the sample production and the beginning of counting and $t_2$ is the time between the sample production and the end of counting.

Substituting Eq. 7 into Eq. 8 yields:

$$C = A_0 \varepsilon(E_\gamma) I_\gamma L (e^{-\lambda t_1} - e^{-\lambda t_2}) \tag{9}$$

And solving for the initial activity, $A_0$, yields:

$$A_0 = \frac{C\lambda}{L\varepsilon(E_\gamma)I_\gamma}(e^{-\lambda t_1} - e^{-\lambda t_2}) \tag{10}$$

Equation 10 can be used to solve for the initial activity of a sample that is counted on a detector with a known efficiency and live time ratio.

Once the initial activity is known the production rate of the radioisotope can be solved for using the solution detailed in Eq. 6:

$$R = \frac{A_0}{1 - e^{-\lambda t_{ir}}} \tag{11}$$

where here $t_{ir}$ is the irradiation time.

Using the counts extracted from Figs. 5b, 6b, 7a, and 7b, the measured live time ratios of those spectra (contained in the caption), and the efficiency calibration given in Fig. 3, the produced activities and production rate of each radioisotope can be calculated. These results are displayed in Tbs. 1 and 2. The uncertainties in these figures were obtained using the general error propagation formula:

$$\sigma = \sqrt{\sum_{i}^{n} \sigma_i^2 \left(\frac{\partial f}{\partial x_i}\right)^2} \tag{12}$$

where $\sigma$ is the uncertainty in the output of the function, $f$, that has $n$ dependent variables, $x_i$, each with an uncertainty, $\sigma_i$.

In this study the uncertainties in the count time and live time ratio variables were assumed to be negligible. The uncertainty in the radioisotope decay constants and gamma intensities are listed in the database from which they were taken [2]. The uncertainty in the efficiency calibration fit was relatively small and was neglected. The uncertainty in the

detector counts was assumed the be statistical and Gaussian in nature, thus the uncertainty in the counts variable is given by:

$$\sigma_C = \frac{\sqrt{C}}{C} \tag{13}$$

| Radioisotope | Activity (Bq) | Production Rate (/s) |
|---|---|---|
| $^{64}$Cu | $2.03 \pm 0.14 \times 10^4$ | $1.12 \pm 0.08 \times 10^6$ |
| $^{67}$Cu | $103 \pm 6$ | $2.75 \pm 0.16 \times 10^4$ |
| $^{88}$Y | - | - |

Table 1: Yields for 30 MeV deuteron run

| Radioisotope | Activity (Bq) | Production Rate (/s) |
|---|---|---|
| $^{64}$Cu | $1.58 \pm 0.10 \times 10^5$ | $8.74 \pm 0.55 \times 10^6$ |
| $^{67}$Cu | $2.34 \pm 0.32 \times 10^3$ | $6.28 \pm 0.86 \times 10^5$ |
| $^{88}$Y | $194 \pm 14$ | $2.15 \pm 0.16 \times 10^6$ |

Table 2: Yields for 50 MeV deuteron run

### 2.3. Production Model

The design of future foil stacks will be tailored solely to radioisotope production and thus will only have a single front foil, a break-up target, and thick back foil. In order to predict the radioisotope production from a design of this configuration, a production model has been developed. This model will be informed by the production rates calculated from the experimental data. The foil stack will be composed of three foils, thus the model will have three components.

As the front foil is meant to produce a radioisotope via a charged particle reaction, it is assumed that the front foil will remain relatively thin such that the deuteron beam can continue on through it. With this assumption in mind, there will be minimal beam depletion and thus the generalized reaction rate ($R$) equation can be used:

$$R = N\sigma x I \tag{14}$$

where $N$ is the number density of the target, $\sigma$ is the microscopic cross section of the production reaction, $x$ is the thickness of the front foil, and $I$ is the beam current.

The activity of the radioisotope in the front foil is then calculated using the previously derived simultaneous production and decay solution given in Eq. 6.

The microscopic cross section of the charged-particle reaction was not ascertained directly from the experiment. Moreover, the reaction cross section will change as the incident particle energy changes. To estimate this energy-dependent behavior, the theoretical nuclear reaction modeling package TALYS can be used [5]. While TALYS will give a decent estimate of the energy-dependent cross section profile, it may not give an accurate estimate of the magnitude of the cross section. To address this, the TALYS predicted energy-dependent cross section

can be normalized to the experimentally measured radioisotope production rate, $R_{exp}$, using the following normalization factor, $a$:

$$a = \frac{R_{exp}}{R_{TALYS}} = \frac{R_{exp}}{N\sigma_{TALYS}xI} \tag{15}$$

where $N$ is the number density of the target, $\sigma_{TALYS}$ is the microscopic cross section of the production reaction as predicted by TALYS, $x$ is the thickness of the front foil, and $I$ is the beam current.

Charged particles lose energy and stop according to the Bragg peak [6]. This means the charged particles will be largely unstopped until they reach their mean range in the material they are traveling. As the first foil is thin, it is assumed the beam depletion through the front foil will be small (only nuclear, and not atomic, interactions), the particle energies will remain largely the same, and effectively the original beam will continue on to impinge on the deuteron break-up target. The angular distribution and energy spectrum of the break-up neutrons is given by a study by Meulders, et al [7]. Figs. 8a and 8b show example data that Meulders, et al. have measured. Meulders, et al. measured break-up neutron energy spectra and angular distributions for 16 MeV, 33 MeV, and 50 MeV deuterons on various materials. When data for deuterons of different energies is required, a linear interpolation of the Meulders data can be used.
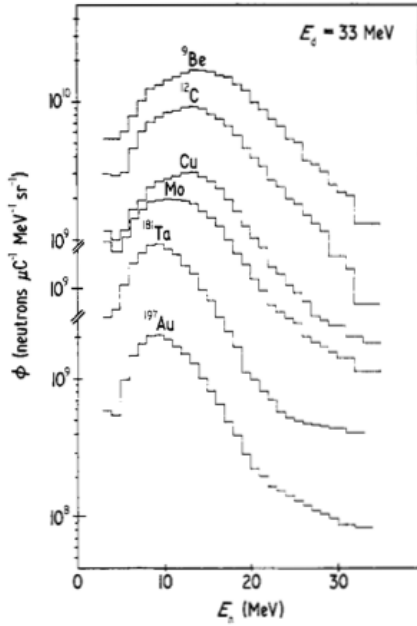


(a) The break-up neutron energy spectrum for 33 MeV deuterons on various materials as measured by Meulders, et al. [7]
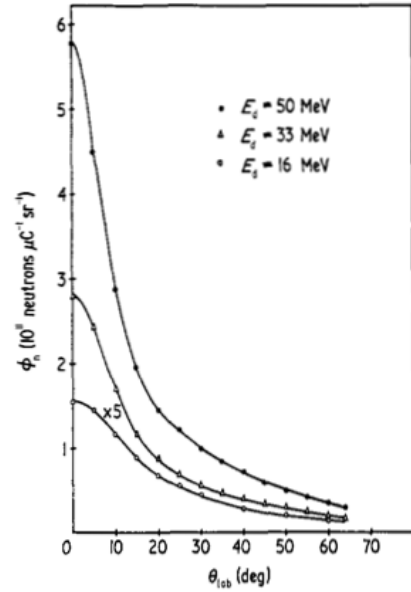
(b) The break-up neutron angular distibution for various incident deuteron energies as measured by Meulders, et al. [7]

The production of radioisotopes in the final stage will be calculated with the general rate equation in Eq. 14. Again Eq. 14 assumes minimal flux depletion through the target.

While the final foil is thick, it is not expected that it will be highly depleting as the break-up neutrons will have high energy (>1 MeV) and high-energy neutrons are highly penetrating in mid to high atomic number material [6]. However, unlike the first foil, the final foil will not be exposed to a unidimensional, monoenergetic beam. The deuteron break-up creates neutrons with a distribution of directions and energies as given by the Meulders data. Therefore, flux must be integrated over the volume of the foil and the cross section must be weighted by the break-up neutron spectrum and integrated with respect to energy:

$$R = N \int_0^\infty \sigma(E_n)P(E_n)\,dE_n \int_V \Phi\,d\theta d\phi dr \tag{16}$$

where $N$ is the number density of the target, $\sigma(E_n)$ is the energy-dependent microscopic reaction cross section, $P(E_n)$ is the break-up neutron energy spectrum, $\Phi$ is the break-up neutron angular distribution.

Using these equations and the experimental data obtained, it will be possible to predict the radioisotope productions in future beam stack designs. Moreover, this model could be minimized to obtain a design that is most likely to produce a specified production of radioisotopes. This model may be used in designs for a future beam stack experiment at the 88 inch cyclotron at Lawrence Berkeley National Laboratory.

## 3. Monte-Carlo Simulations - Isaac Meyer

### 3.1. Simulation Set-Up

Previously in the paper, an analytical model for estimating the isotope production was presented. Another way of estimating the level of isotope production is by running physics simulations of the design to determine the flux and energy of particles at key points of the beam stack. The simulations run for this work were done in MCNP[8] with the details outlined in the next paragraph.

The model for these initial simulations was based on the initial set-up of the experiment. The stack was modeled as a cylinder with radius of 2.0 cm. The three stages were composed of the following materials and thicknesses:

| Stage | Material | Thickness (mm) |
|-------|----------|----------------|
| 1     | Zr       | 0.025          |
| 2     | Be       | 3.0            |
| 3     | Zn       | 30.0           |

The source of deuterons in the problem was defined as uniformly distributed on a circle of radius 3.25 mm located 1.0075 cm to the left stack. This matches the beam spot of the experiment. Deuterons were sourced with initial trajectories parallel to the x-axis in the positive x-direction. A diagram of the problem set-up can be seen in Fig. 9.
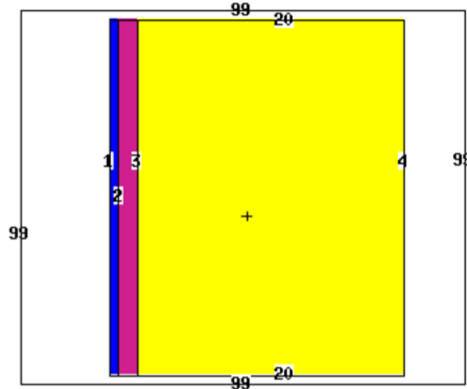
11

Figure 9: Problem Set-Up

### 3.2. Initial Results of MCNP

The initial results of the simulation for various particles can be seen in Fig. 10. These initial results match the qualitative understanding of the system previously proposed. For deuterons, not much attenuation is expected in the first layer because its thickness is less than where the Bragg peak to occur in that material. The simulation shows that most deuterons are attenuated in the second stage and that none make it past the first stage. The neutron spectra also follow the expected trend. There is a small amount of break-up neutrons after the first stage, the largest amount after the second stage, and then those neutrons are mostly attenuated in the third stage.

While protons are not being used to produce any medical isotopes in this system, the flux of those particles is also important to estimating the levels of undesirable isotopes produced. Again, the proton flux follows intuition: there is a small amount after the first stage, a larger amount after the second stage, and they are completely attenuated by the third stage.

### 3.3. Varying a Parameter

To probe some of the possible variations of the design, simulations were run in which the width of the first layer were adjusted. For each of these changes, the simulation produced a prediction of the flux of neutrons in the first stage and neutrons in the third stage. These were chosen as the thicknesses because, as stated before, the goal is to produce isotopes by a $(D, x)$ reaction in the first stage and an $(n, x)$ reaction in the third stage. The results of varying the width of the first stage on these specific spectra can be seen in Fig. 11.

These results also reflect the intuition of the changes an increased thickness in the first layer would cause. While the total deuteron flux is not drastically changed, the increase in the width of the first layer will drastically broaden out the deuteron energy spectrum. With a thicker first layer, a lower flux of neutrons would be expected in the third stage, and this can be seen in the simulation. One important thing to note here is the difference in magnitude of these plots. The deuteron graph is plotted in log scale on the y-axis and has many parts of the spectrum that approach 1.0 (deuterons/source deuteron). The neutron spectra are plotted with a linear y-axis and occur on a much smaller scale: around 0.003

12

(a) Deuteron Flux

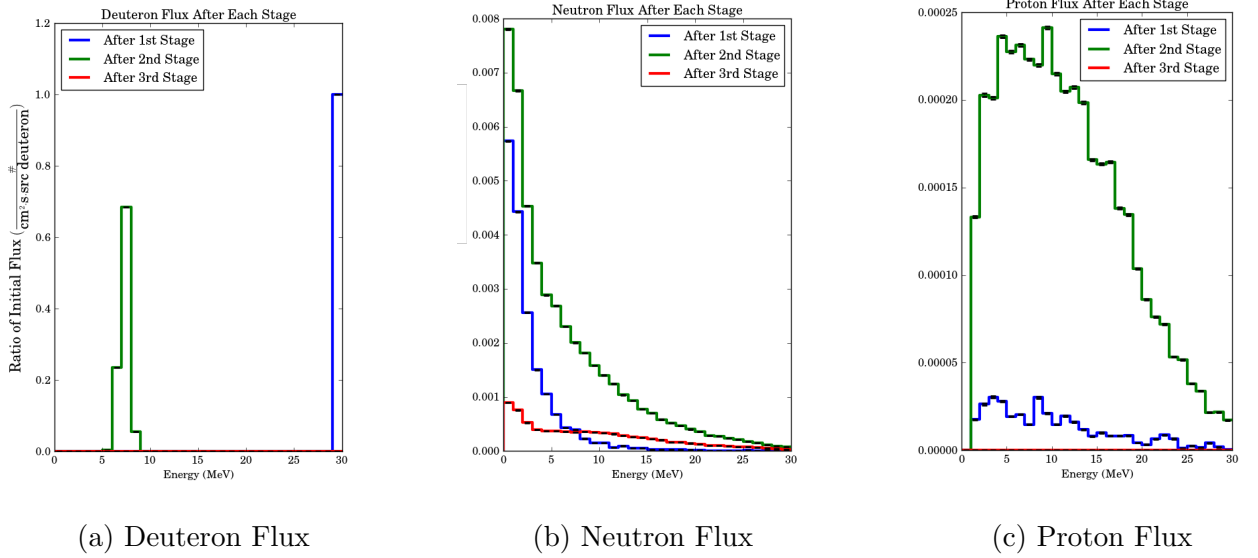(b) Neutron Flux

(c) Proton Flux

Figure 10: Shown is the spectrum of each particle after the first stage (Blue), second stage (Green), and third stage (Red).

(deuterons/source deuteron). This brings up the important question of efficiency of the production of isotopes via neutrons in this design and merits further analysis.
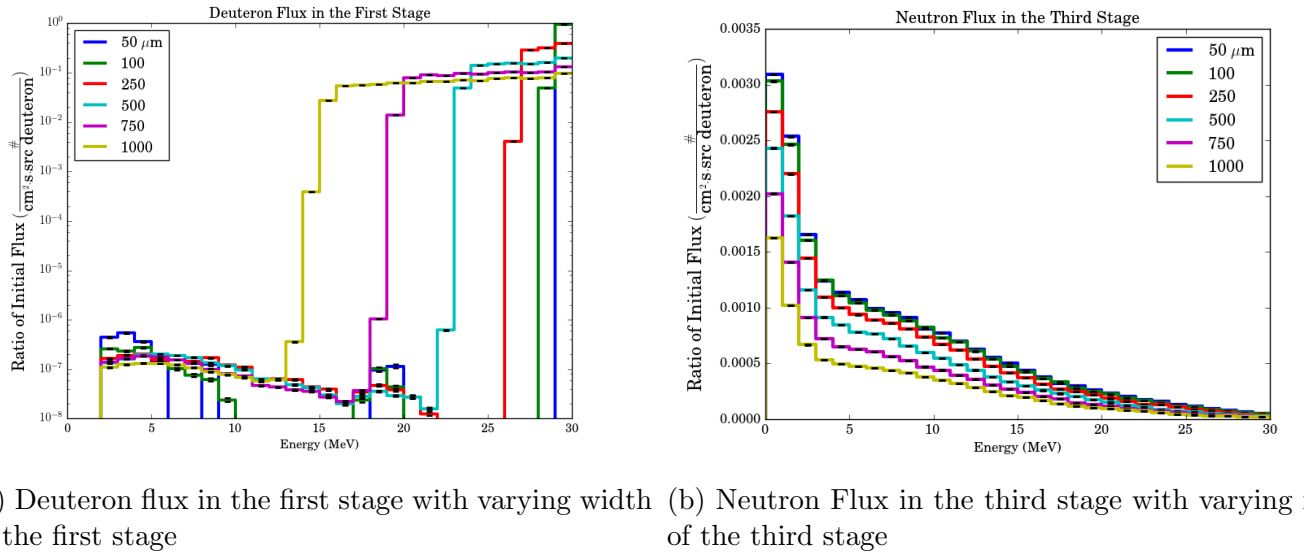


(a) Deuteron flux in the first stage with varying width of the first stage

(b) Neutron Flux in the third stage with varying flux of the third stage

Figure 11: Spectra of interest in the first and third stages

### 3.4. Possible Improvements of Model

While this exercise initially provided an insight into the ability to model the physics of the problem, there is clearly much work that needs to be done to expand the capability of

13

this design. The spectra that were studied in this work were not actually convolved with the experimental cross-sections for the isotopes of interests. Conducting this final step would yield an estimate of the amount of each isotope produced.

Improvement of the simulation could also come through verification and selection of the nuclear data used. MCNP was initially designed for neutron transport and is therefore not always a reliable source for more exotic applications such as this.

Another step that might be taken to improve the prediction of yield through radiation transport is using the GEANT4 Simulation Toolkit [9]. Initial work for this aspect of the project was begun in GEANT4 but switched to MCNP because of the designer's familiarity with the latter code. Constructing this geometry in GEANT4 would likely allow for more control over the interaction models being used and more easily tagging events of interest (i.e. only those which produce isotopes). Another development that is desirable is the ability to easily adjust the width of each stage. The method used in the current work was to edit the input files to re-run the simulation, but one can easily envision a GUI which allows a user to input their custom dimensions and run the program to produce an expected yield utilizing those dimensions. This would grant the ability to preferentially increase production in a specific stage based on current demand and capabilities of their medical facility.

## 4. Material Selection and Considerations - Evan Still

### 4.1. Material Constraints

In order to convert the transmitted deuteron beam from the front foil into the neutrons for zinc transmutation a medium must be used to facilitate excitation and subsequent break-up of the deuterons. During the breakup process the incident deuterons are able to displace atoms, deposit heat, and transmute the break-up target into various contaminant elements.

Due to the displacement of atoms within the lattice, the structure of the target can be compromised through the effects of radiation embrittlement, resulting in a higher strength but less ductile material. To account for these effects a material must be chosen with high resistance to radiation-induced embrittlement such that fracture can be prevented during operation. Alternatively, if no suitable materials can be identified the stage must be designed to minimize any produced stress in the structure.

The effect of the deposited heat on the target can lead to melting, annealing, and volumetric expansion, each leading to a different failure criterion for the system. The effect of annealing will result in an average decrease in yield and fracture stress as new crystals nucleate, removing the effects of dislocation based strengthening mechanisms thus causing fracture prior to the expected stress levels. Volumetric expansion of the target results in an applied stress on both the target and the beam box that all the components are housed in as the beam box confines the expansion in two of the three axes. In order to account for heating, a material must possess high melting points to raise the initiation temperature for the annealing process and prevent melting, while high heat conductivity is required in order to dissipate the heat to attain a stable temperature for operation.

The break up of deuterons into neutrons has been shown to be proportional to the electron density of the target material [7]. As such the optimal target materials will be in

14

the upper-right portion of the periodic table, as these elements have high electronegativity and high electron density. Given the above constraints the following materials were selected for investigation as the break-up target: beryllium, graphite, silicon carbide, and aluminum.

## 4.2. Mechanical Theory

In a one dimensional, idealized design the stress, $\sigma$, of a material is linked to the strain (elongation) for a material through the Young's modulus. The stress can be expressed as the force per unit area as shown in Equation 17 [10], where $\sigma$ is the stress in units of pascals, $P$ is the force in units of newtons, and $A$ is the area in units of square meters. Equation 18 [10] shows that strain, $\epsilon$, is the percent elongation of a material dependent on the initial length and the final length. Equation 19 [10] depicts the relationship between the two parameters with $E$ being the Youngs modulus in units of pascals.

$$\sigma = \frac{P}{A} \tag{17}$$

$$\epsilon = \frac{L_F - L_0}{L_0} = \frac{\Delta L}{L} \tag{18}$$

$$E = \frac{\sigma}{\epsilon} \tag{19}$$

From these three relationships, the three dimensional case can be derived in the form of Hooke's law for an isotropic material (Eq. 20 [10]) with the inclusion of Poisson's ratio to account for the effects of stress that are not collinear with the direction of the strain.

$$\epsilon_{ij} = \frac{1}{E} \left( \sigma_{ij} - \nu \left( \sigma_{ij} \delta ij - \sigma_{ij} \right) \right) \tag{20}$$

In order to use Hooke's law to determine the full stress state the system's constraints must be used to determine a set of known stresses and strains. The effect of the deuteron beam on the stress state is that of thermal shock and thermal expansion. There are two cases for the break-up target. Case 1 exists when the break-up target areal cross section is at a maximum of 5×6 cm, while Case 2 exists when the beam stop will have a cross section less than 5×6 cm at maximum expansion.

### 4.2.1. Case 1

Let the principal directions for the system be defined as the 11, 22, and 33 directions. Case 1 limits the direction of thermal expansion to be along the 11 direction as expansion of the other two dimensions is prevented by the beam box. In the case of the unidirectional expansion the strain is given by Eq. 21 [10].

$$\epsilon = \alpha \Delta T \tag{21}$$

Where $\alpha$ represents the coefficient of linear expansion in units of K$^{-1}$, while $\Delta$T is the change in temperature. For the confined case the strain will be zero and a stress is instead developed according to Eq. 22 [10].

15

$$\sigma = E\alpha\Delta T \tag{22}$$

In case 1, the strain in the 22 and 33 directions will be zero and the stresses will be given by Eq. 22. With these four known parameters the stresses and strain in the 11 direction can be calculated, resulting in Eqs. 23 and 24.

$$\sigma_{11} = E\alpha\Delta T \left(\frac{1}{\nu} - 1\right) \tag{23}$$

$$\epsilon_{11} = \alpha\Delta T \left(\frac{1}{\nu} - 1 - 2\nu\right) \tag{24}$$

In order to determine the yielding criterion the Von Mises approach is applied. The Von Mises approximation is valid for the case of tensile loading and is used to calculate an equivalent stress from loading in the principal directions which can then be compared to the yield stress for a material. The Von Mises criterion for loading in the principal directions is given in Eq. 25 [10], while the modified form for the constraints is provided in Eq. 26.

$$\sigma_{VM} = \sqrt{\frac{1}{2}\left((\sigma_{11} - \sigma 22)^2 + (\sigma_{22} - \sigma 33)^2 + (\sigma_{33} - \sigma 11)^2\right)} \tag{25}$$

$$\sigma_{VM}^1 = \sqrt{\frac{1}{2}\left(\left(E\alpha\Delta T\left(\frac{1}{2} - 2\right)\right)^2 + \left(E\alpha\Delta T\left(2 - \frac{1}{2}\right)\right)^2\right)} \tag{26}$$

### 4.2.2. Case 2

In Case 2, the break-up target is designed such that the expansion of the target will not result in contact with the beam-box and thus the development of large stresses. As such the initial condition is that the principal strains are all according to Eq. 22. When solving this system of equations, the final result is that all three stresses are equivalent and given in Eq. 27.

$$\sigma_{11} = \sigma_{22} = \sigma 33 = -\frac{E\alpha\Delta T}{2\nu - 1} \tag{27}$$

Using the Von Mises criterion from Eq. 25 shows that as the three stresses are equivalent, thus the Von Mises stress is zero and yielding will not occur during normal operation. This comes at the cost of a reduced area for the target. By using Eq. 21 the limits on the foils height and width can be calculated and plotted as a function of temperature to maintain this condition.

### 4.3. Deuteron Interactions in the Beam Stop

SRIM® is a program used to model charged particle interactions in matter [11]. SRIM® enables the selection of ion parameters such as mass and energy as well as target properties

including thickness, density, and atomic percentage for different atoms. By modeling individual ions traveling through the selected targets SRIM® is able to determine the average range for a given ion as well as the vacancies the ion produces along its flight path by looking at the energy loss due to electronic interactions. It is important to note however that SRIM® cannot accurately generate data on the attenuation of ions through a medium as it ignores the effects of nuclear interactions such as absorption.

In order to determine the required thicknesses for each candidate material SRIM was run several times from a 10 MeV deuteron beam to a 50 MeV beam with 5 MeV step sizes. For each case, 5000 ions were generated and the thickness in the SRIM® model was increased until no deuterons were transmitted through the structure. Once the correct thickness was determined for each energy a 10000 ion run was commenced to determine the average number of vacancies produced per ion per angstrom, VIA. VIA is a SRIM® output which depicts the number of atomic vacancies produced by each ion along its path through the medium. This measurement can be correlated to the displacement per atom, DPA, through Eq. 28 [12], which is a standard for comparing materials' radiation resistance.

$$DPA = VIA\frac{\phi}{N_A}t \tag{28}$$

In Eq. 28, VIA represents the Vacancies per Ion per Angstrom, while $\phi$ is the flux in deuterons per s per $cm^2$, $N_A$ is the atomic density, and t is exposure time in seconds. For the comparison of the candidate materials the time component was left as an unknown dependent on the desired pulse time. The displacement rate per atom and time to reach a DPA of 1 were used.

### 4.4. Results

Table 3 below has the necessary parameters for the comparison of the mechanical and SRIM properties between the candidate materials. From Tb. 3 the coefficient of thermal expansion, $k$, the Young's modulus, E, and Poisson's ratio, $\nu$, are used to determine the Von Mises Stress and compared to the yield stress for the mechanical Cases 1 and 2.

Table 3: Material Properties

| Material | Zr [13] | Zn [14] [15] | Graphite [16] | Be [17] | SiC [18] | Al (6000 Series) [19] |
|---|---|---|---|---|---|---|
| k $(\frac{W}{mK})$ | 16.7 | 112.2 | 8.7-114 | 216 | 3.8-20.7 | 130-226 |
| $\alpha$ $(\frac{\mu m}{mK})$ | 5.7 | 30.2 | .6-5.2 | 12 | 7.1-11 | 24 |
| E (GPa) | 94.5 | 108 | 5.99 | 5.985 | 5.996 | 67-140 |
| $\nu$ | .34 | .25 | 4.9925 | 4.987 | 4.997 | .30-.330 |
| Yield (MPa) | 230 | | 4.8-76 | 240 | 240-1625 | 40-490 |
| Melting Point (K) | 2128 | 692.68 | 3923 | 3923 | 1750-1955 | 933.37 |

### 4.4.1. Mechanics

The results of the Case 1 mechanical analysis for the four candidate materials and the two irradiated foils, zinc and zirconium is displayed below in Figs. 12a and 12b.

17
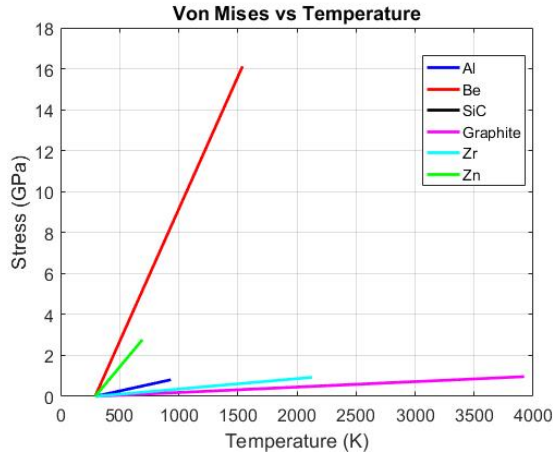
(a) Von Mises Stress as a function of tempera-
ture.
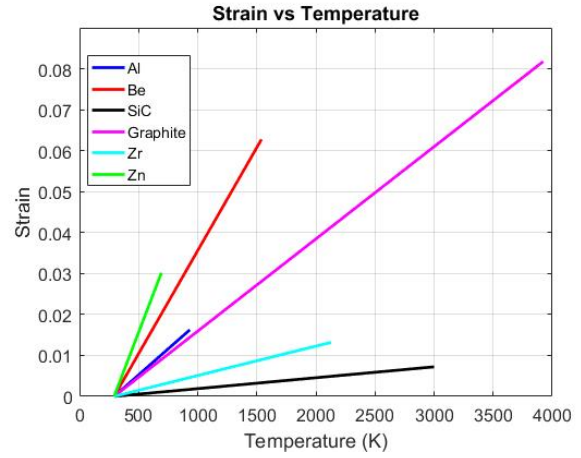
(b) $\epsilon_{11}$ as a function of temperature.

Figure 12: Case 1 Mechanical Response

From Fig. 12a it is seen that a beryllium beam stop surpasses its yield stress of 240 MPa by a temperature of 312 K. For the Al 6000 series the composite with the lowest yield stress will be surpassed at 325 K while its maximum yield stress is not surpassed until 680 K. In a similar fashion to the Al, SiC yields at 1200 K for its minimum stress and does not yield prior to melting if designed for the maximum yield stress. A graphite beam stop surpasses its minimum and maximum yield criterion at temperatures of 323 K and 580 K, respectively. Figure 12b shows that the SiC undergoes the least expansion in the 11 direction while the beryllium undergoes the most.

In Case 2, since the Von Mises criterion results in zero stress, instead the minimum dimensions needed to prevent collision with the beam box is calculated and graphed in Fig. 13.

Figure 13 shows that out of the candidate materials at a set temperature prior to melting aluminum requires the greatest reduction in the area of the beam stop while SiC requires the least reduction to maintain valid conditions for Case 2.

### 4.4.2. SRIM

The range and displacement rate per atom is presented in Fig. 14. It is evident from Fig. 14a that Be requires the largest distance to stop all incoming deuterons while SiC is most efficient. Contrary to the range data, Be undergoes the lowest displacement rate for all deuteron energies while SiC experiences the highest displacement rate according to Fig. 14b. For a 50 MeV deuteron beam the time required to reach a dose of 1 DPA is determined to be; 3.02, 14.78. 4.9, and 17.99 years for SiC, graphite, Al, and Be, respectively.
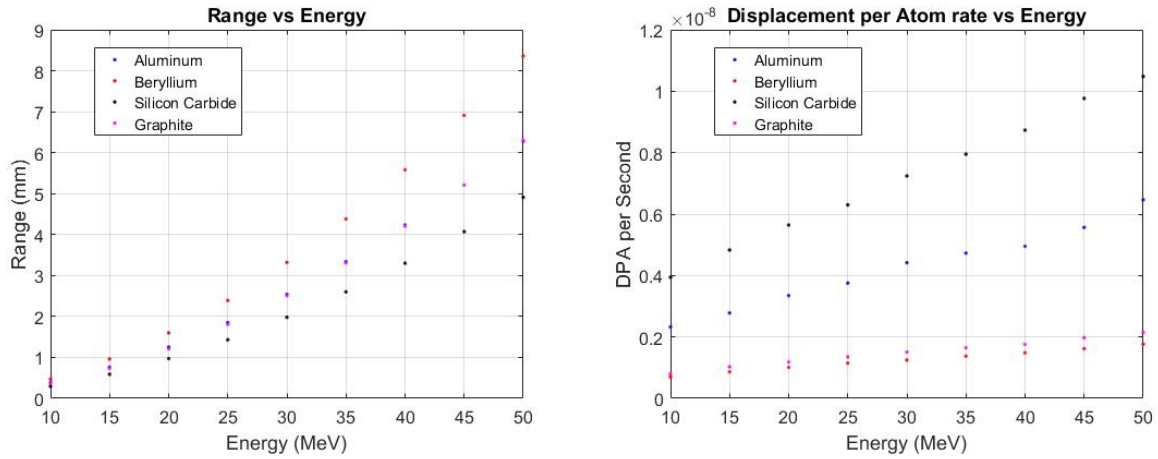
### 4.5. Materials Comparison

The analysis results are presented in Tb. 4 where the best parameters in each category are bolded.At initial glance SiC and graphite appear as the two optimal candidate materials.
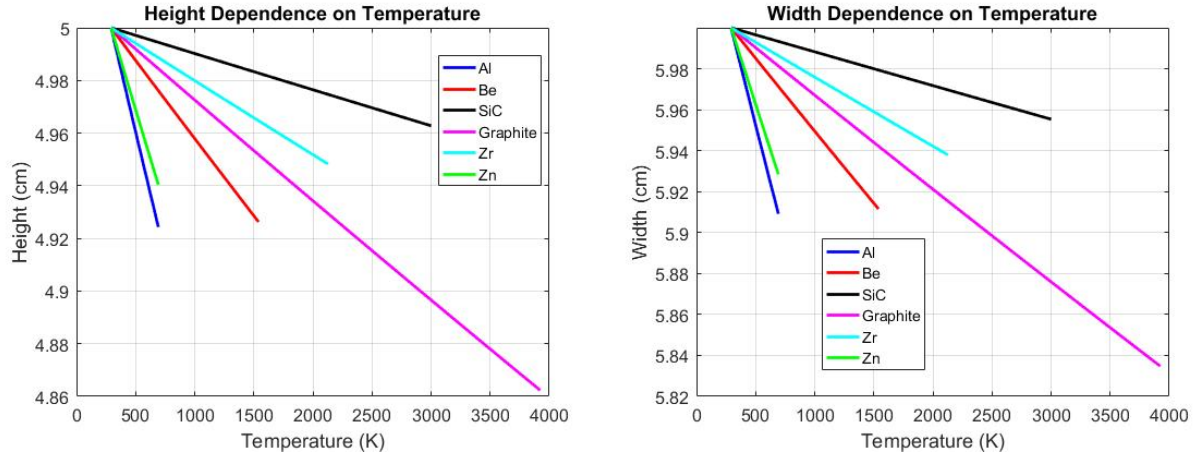
(a) Maximum height as a function of temperature.



(b) Maximum width as a function of temperature.

Figure 13: Case 2 Dimensional Constraints



(a) Deuteron range as a function of energy.



(b) Displacement Rate as a function of Energy.

Figure 14: SRIM Outputs with Energy Dependence

With SiC possessing the best mechanical properties for Case 1 and the lowest deuteron range. Graphite possesses the highest electronegativity, melting point, and thermal expansion in the 11 direction. The mechanical constraints of Case 1 are avoided using Case 2, resulting in a safer system. The advantage of SiC's mechanical properties are of lesser importance when compared to the graphite's electronegativity and melting point. Thus graphite is the optimal material for the deuteron breakup target as it is not a structural component.

## 4.6. Stage Design

SOLIDWORKS® was used to design a stage assembly for insertion into the current beam box used at the 88 inch cyclotron at Lawrence Berkeley National Lab. Exploded and non-

19

Table 4: Material Selection Parameters

| Material | Graphite [16] | Be [17] | SiC [18] | Al (6000) [19] |
|---|---|---|---|---|
| Deuteron Range at 30 MeV (mm) | 2.51 | 3.32 | **1.98** | 2.54 |
| DPA rate at 30 MeV | $1.5x10^{-9}$ | $1.25x10^{-9}$ | $7.2310^{-9}$ | $4.410^{-9}$ |
| Case 2: Maximum Width at 500 K (cm) | 5.99 | 5.985 | **5.996** | 5.952 |
| Case 2: Maximum Height at 500 K (cm) | 4.9925 | 4.987 | **4.997** | 4.96 |
| Case 1: Strain 11 at 500 K | $4.65x10^{-3}$ | $1.0410^{-2}$ | $5.510^{-4}$ | $5.2510^{-3}$ |
| Case 1: at 500 K (MPa) | **23** | 2500 | 55 | 260 |
| Yield Strength (MPa) | 4.8-76 | 240 | **240-1625** | 40-490 |
| Electronegativity | **2.55** | 1.57 | 2.3 | 1.61 |
| Melting Point (K) | **3923** | 1540 | 1750-1955 | 933.37 |

exploded views of the stage assembly with example targets are presented in Fig. 15, where the stage is machined from a $25\times6\times2$ cm$^3$ aluminum block. The foils are locked in place via two aluminum rods of diameter, .48 cm, and length 23.5 cm. The aluminum rods slide into position through a set of diameter, .50 cm, holes visible in Fig. 15c, which are stabilized by a set of four M2 socket head cap screws. Using the results from Fig. 13 the final dimensions for the Zr, graphite, and Zn foils, are .025$\times$5$\times$4.995 cm$^3$, .24$\times$5$\times$4.996 cm$^3$, and 10$\times$5$\times$4.997 cm$^3$. The use of the aluminum rods and set screws enables the design to have exchangeable foils while isolating the foil movement in three dimensions.

## 5. Heat Transfer Simulations - Eliav Maas

### 5.1. Heat Transfer Background

COMSOL Multiphysics® was used to in order to model the heat transfer which occurs in then design [20]. As an ion beam penetrates through a solid medium many competing mechanisms for energy transfer occur. Energy is dissipated by the incident particles through the inelastic scattering of incident ions off the solid medium as the beam is attenuated and penetrates further into the target. Energy transfer also occurs due to the nuclear interactions occurring within the medium. Depending on the specific reaction energy is either absorbed or released by these interactions.

A few simplifying assumptions were made in order to effectively model the system and take advantage of the tools available in COMSOL's® heat transfer module package. The effects of convective heat transfer were ignored because the apparatus undergoes deuteron bombardment in near vacuum conditions. The focus of this simulation was therefore on the conductive and radiative heat transfer which occurs in the system. COMSOL's® Deposited Beam Heat function was implemented as a conservative estimate for the power deposited by the incident particle beam on each foil of the system. In reality the heat would be dissipated as the particle beam is attenuated through the foil but this simplification assumes all heat from the beam is dissipated within a very short penetration depth into the foil. This simulation informs the highest temperature hot spot and surrounding temperature profile
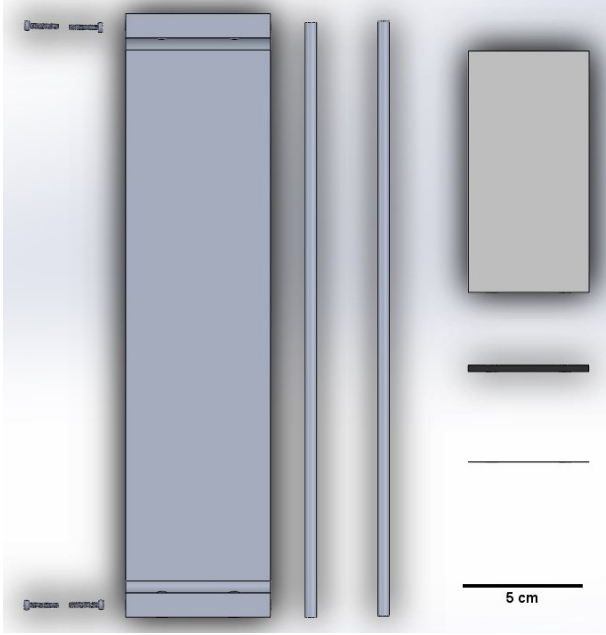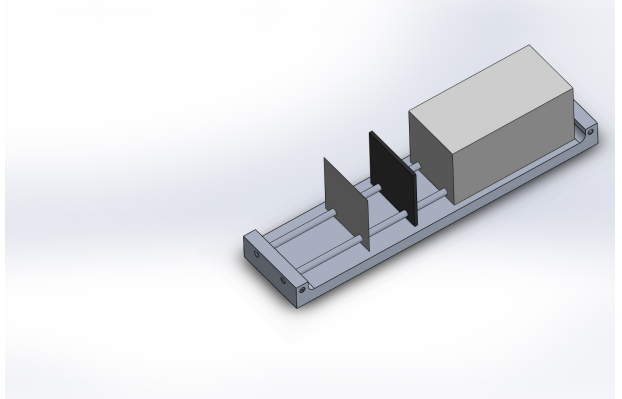
(a) Exploded View 1.
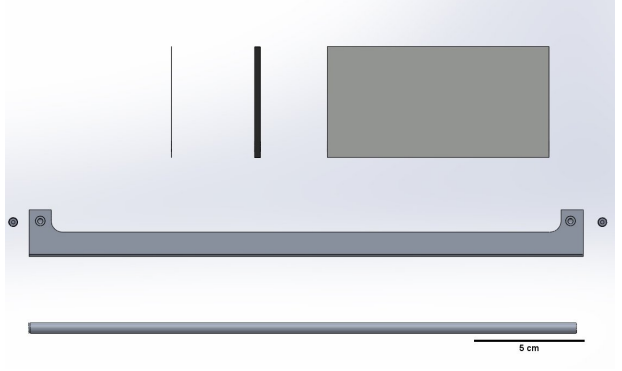
(b) Exploded View 2.
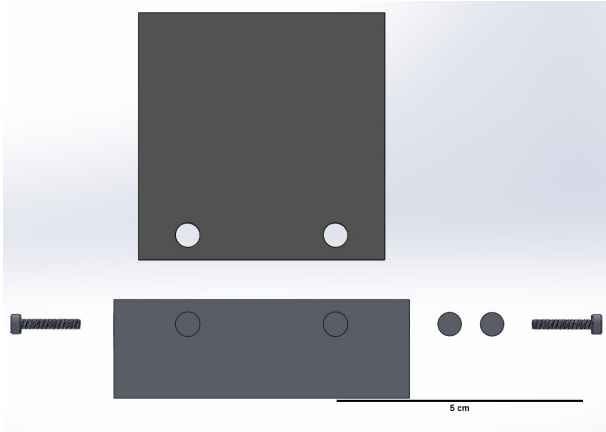
(c) Exploded View 3.

(d) Nonexploded View

Figure 15: Stage Assembly with Example Foils

that could form in the system. This information can guide the design of the individual foils used, the safe beam current, and the safe irradiation time used for isotope production.

Assuming a steady state particle flux and average energy of each species, an energy balance can be performed over the individual foils in order to calculate the power, $P$, deposited in each as follows:

$$P_{deposited,i} = \frac{\partial E_i}{\partial t} = \sum_j [I_{in,i,j} \bar{E}_{in,i,j} - I_{out,i,j} \bar{E}_{out,i,j}] \tag{29}$$

where $I$ is the current of particles (number of particles per second) and $\bar{E}$ is the average

energy per particle. The subscripts $i$ and $j$ denote the foil and species being analyzed respectively.

Given an initial beam current and average energy, the attenuation of the beam through the different materials was modeled using the Bethe-Bloch Stopping Power formula [6]:

$$\frac{dE}{dx} = \frac{4\pi n_e z}{m_e v^2} \left( \frac{e^2}{4\pi\epsilon_0} \right)^2 \left[ ln \left( \frac{2m_e v^2}{10eV(Z)} \right) \right] \tag{30}$$

where $Z$ is the target atomic number, $z$ is the incident particle atomic number, $n_e$ is the target electron density, $v$ is the incident particle velocity, $m_e$ is the electron mass, $e$ is the electron charge, and $\epsilon_0$ is the permittivity of free space.

By numerically integrating Eq. 30 over the length of the foil of interest, $L$, an average energy lost by the beam through the foil can be approximated. This change in energy can then be subtracted from the initial energy in order determine the average particle energy after passing through the foil as such:

$$\bar{E}_f = \bar{E}_0 - \int_0^L \frac{dE}{dx} dx \tag{31}$$

The ratio of the final to initial particle energy will be roughly equal to the ratio of final to initial beam current:

$$\frac{\bar{E}_f}{\bar{E}_0} \approx \frac{I_f}{I_0} \tag{32}$$

This method was used to calculate values for current and average particle energy which could then be used in order to implement a model of the full system in COMSOL® as detailed in the following section.

5.2. Model Implementation

As previously mentioned, the COMSOL® Deposited Beam Heat Function was used to simulate the deuteron beam. Deposited Beam Heat simulates the heat deposited when a laser beam hits a material. The inputs to this function are the beam origin point, the orientation of the beam, and the amount of power deposited into the material by the laser. Because the system is being modeled in a vacuum the the distance from the beam's origin point to the foil does not effect the simulation, as beam spreading will not occur. The beam was oriented perpendicularly to the foil for all simulations. Equation 29 was used to calculate the the power deposited in each foil.
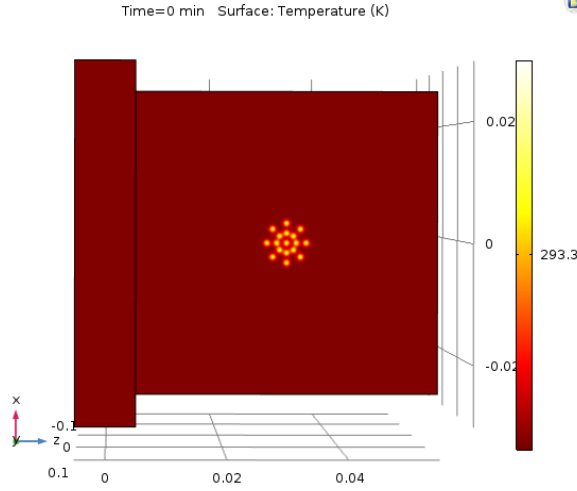
Figure 16: COMSOL® deposited beam heat points oriented in three concentric circles. These 17 points were used to simulate deuteron beam spot.

In order to better simulate the distribution of ions on the foil, the beam was split into many lower power beams which were oriented in concentric circles around the middle of the beam spot. Two concentric circles with eight points each were oriented around the middle beam spot, leading to 17 total beam spots. The outer circle had a radius of 0.325 mm, similar to the experiment preformed at LBNL. This configuration of points can be seen in Fig. 16. Adding more points made a negligible difference in terms of the overall temperature profile generated using COMSOL®.

The effect of proton and neutron heating was neglected as it would be quite low. Therefore, only deuteron heating was considered. It was determined using Eq. 31 that after the deuteron beam is slightly attenuated in the zirconium first foil and that it is fully stopped in the second foil (break-up target). This result was found for both 30 and 50 MeV deuteron beams. The amount of beam attenuation for both 30 and 50 MeV deuteron beams through a 25 $\mu$m zirconium foil are summarized in Tb. 5.

| $E_0$ [MeV] | $I_f$ | $\bar{E}_f$[MeV] |
|---|---|---|
| 30 | $0.990 \cdot I_0$ | 29.7 |
| 50 | $0.996 \cdot I_0$ | 49.8 |

Table 5: Beam attenuation for both 30 and 50 MeV deuteron beams through a 25 $\mu$m zirconium foil. Calculated using Eqs. 30, 31, and 32.

In these simulations the optimum material chosen in Sec. 4.5 (graphite) was used for the beam stop. The two values for each simulation that must be calculated are the power deposited in the zirconium foil and graphite beam stop. The values for the $P_{deposited}$ for the various beam currents and energies simulated are summarized in Tb. 6. The choices with regards to specific currents examined are explained in Sec. 5.3

23

| Beam Current | Beam Energy [MeV] | $P_{deposited,Zr}$ [W] | $P_{deposited,C}$ [W] |
|---|---|---|---|
| 100 nA | 30 | 0.0587 | 2.94 |
| 2.5 $\mu$A | 30 | 1.47 | 73.5 |
| 100 nA | 50 | 0.0393 | 4.96 |
| 3.5 $\mu$A | 50 | 1.38 | 174 |

Table 6: Power deposited in the zirconium first foil (denoted Zr) and graphite beam stop (denoted C) for various deuteron beam currents. Calculated using Eq. 29.

The three foils were simulated with a length and width of 5 cm. The thickness of the individual foils are shown in Tb. 7. The base was modeled as a 1 cm by 6 cm by 20 cm aluminum block.

| Zirconium Thickness | Graphite Thickness | Zinc Thickness |
|---|---|---|
| 25 $\mu$m | 2.6 mm | 10 cm |

Table 7: Thicknesses used for individual foils in COMSOL® simulations.

## 5.3. Heat Transfer Results and Discussion

Using the $P_{deposited}$ values found in Tb. 6, COMSOL® simulations of various situations were run. First, the beam current run in the LBNL experiment (100 nA) was examined. The temperature profile for a 30 and 50 MeV deuteron beam after 20 minutes of irradiation can be seen in Figs. 17a and 17b, respectively.
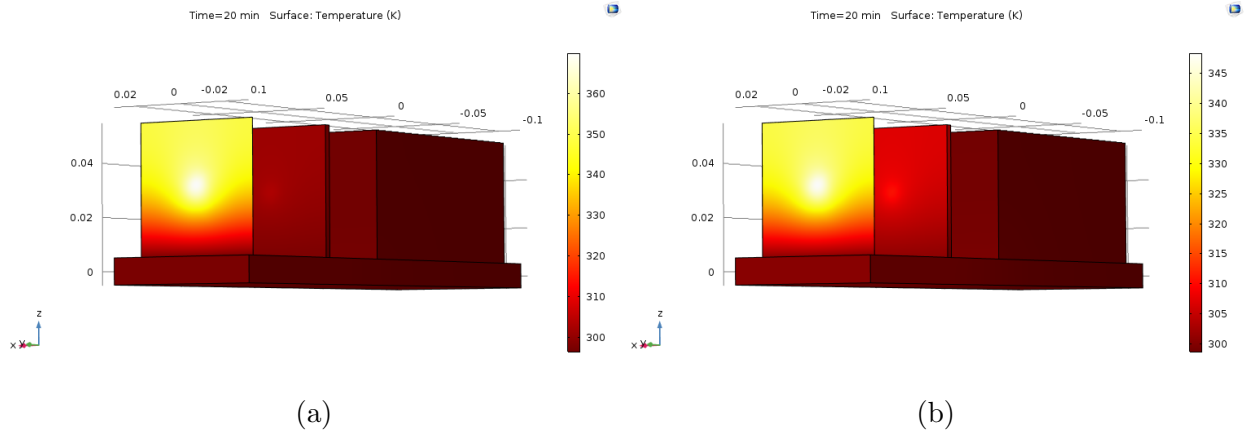


Figure 17: Surface temperature profile of full system being bombarded by a 30 MeV (a) and 50 MeV (b) deuteron beam run at 100 nA. Both simulations were run for 20 minutes.

These simulations at 100 nA indicate that there are no safety concerns with regards to our system at such low currents. The maximum temperature for both situations occurs on the zirconium foil and are below 400 K. This is well below the melting point of zirconium (about 2100 K).

24

The hottest point on the graphite beam stop and zirconium foil are plotted as a function of time in Figs. 18a and 18b, respectively. This plot reveals an unintuitive result. When the thin zirconium foil bombarded with a 30 MeV deuteron beam it heats up more than when it is bombarded with a 50 MeV deuteron beam. This is because the higher energy particles are moving faster and thus are not attenuated as well by the foil. Thus more pass through the foil without depositing energy. Because the graphite absorbs the balance of energy, the 50 MeV beam still heats up the graphite more than the 30 MeV beam.
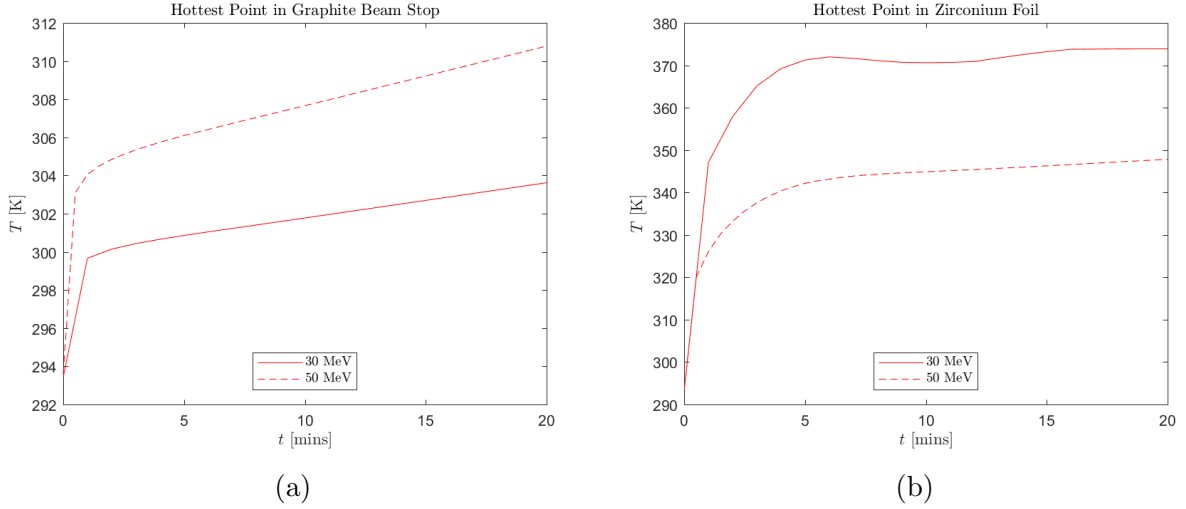


Figure 18: The hottest point on the zirconium foil (a) and graphite beam stop (b) plotted over 20 minutes of bombardment by a 30 MeV (solid line) and 50 MeV (dashed line) deuteron beam

The next objective was to find the current limit at each of these beam energies that would still result in safe operation of the device. The zirconium foil heats faster and has a much lower melting point than graphite (about 2100 K versus 4000 K) so the beam current at which the zirconium foil is close to melting was determined. As a conservative estimate the current limit was defined to be the current at which the zirconium foil reaches 1900 K after 20 minutes of beam irradiation. The summary of current limits found can be seen in Tb. 8 and the corresponding surface temperature profiles can be found in Figs. 19a and 19b for the 30 and 50 MeV cases, respectively.

| $\bar{E}_0$ [MeV] | Current Limit [$\mu$A] |
|---|---|
| 30 | 2.5 |
| 50 | 3.5 |

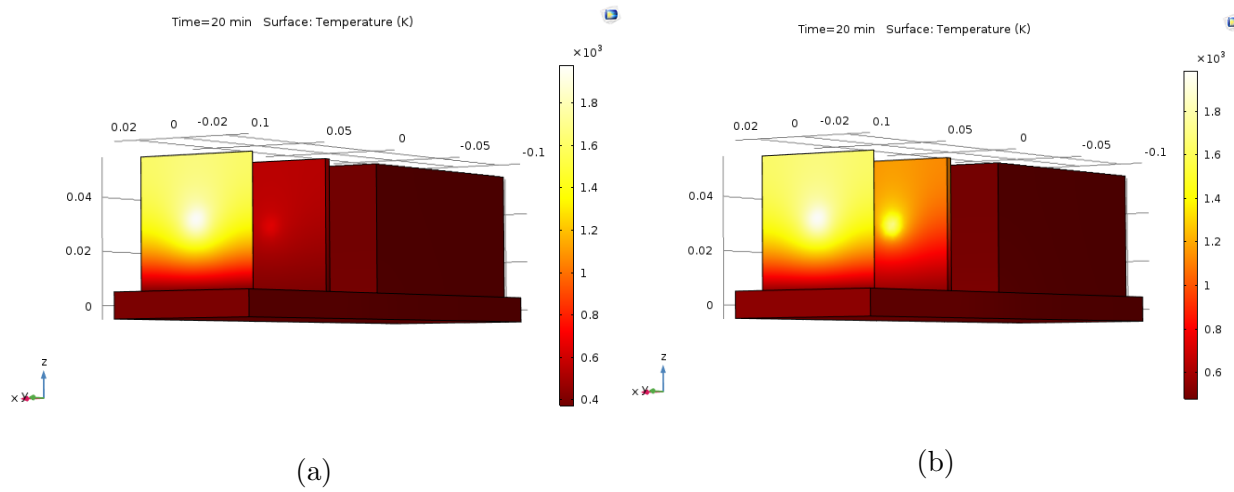Table 8: Maximum current for safe operation with 25 $\mu$m zirconium foil after 20 minutes of beam irradiation.

25

Figure 19: Surface temperature profile of full system being bombarded by a a 30 MeV deuteron beam run at the current limit of 2.5 $\mu$A (a) and a 50 MeV Deuteron beam run at the current limit of 3.5 $\mu$A (b). Both simulations were run for 20 minutes.

## 6. Chemical Separation - Joe Corvino

### 6.1. Separation Methods

The copper ($^{64,67}$Cu) and yttrium ($^{88}$Y) radioisotopes have promising therapeutic and diagnostic properties [1, 21]. These radioisotopes can be ingested or injected into the human body if they are in the form of a salt (i.e. $CaCl_2$) or attached to an acceptable organic ligand. The specific method of transporting the radioisotope to the human body, and the molecular form of the radioisotope, is beyond the scope of this project: these decisions often require years of research and testing [1, 21]. Regardless of their molecular form, the Cu and Y must first be separated and sufficiently purified. There are two common separation methods that were examined in this design project: the first is electrochemical separation and the second is ion exchange chromatography.

### 6.1.1. Electroplating

Electroplating is a process by which metal cations are deposited on an electrode. A schematic of a typical electroplating setup is shown below in Fig. 20.
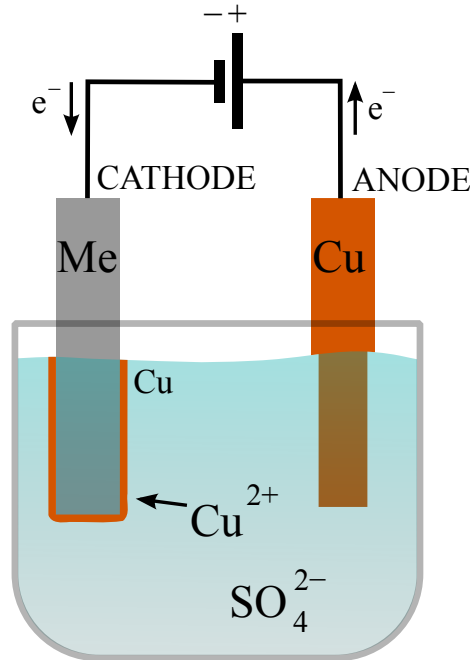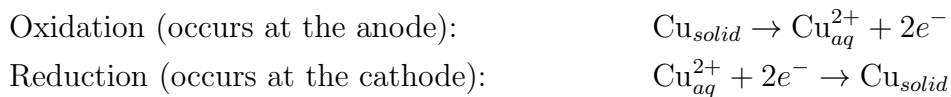
26

Figure 20: Diagram of electroplating process. A voltage potential is applied to a metal (Me) cathode and copper (Cu) anode. The dissolved copper in the solution is chemically reduced and attaches to the metal surface. This process is called electrodeposition (a.k.a. electroplating). The solid copper anode is oxidized and leaches into the acidic solution. *Figure adapted from Wikipedia* [22].

The radioactive copper is present in the acid solution from the dissolution of the zinc foil. As shown in Fig. 20, the radioactive copper in the solution would deposit on a metal surface (such as silver) [22]. However, as the radioactive copper is removed from the solution, non-radioactive copper would be introduced into the system from the copper anode. Eventually, the radioactive Cu-64,67 will be substantially diluted by the natural copper (*natural* indicates that the isotopic composition is the same which is found in nature, i.e. it has not been enriched or irradiated).

The reduction and oxidation of the copper follows the reactions [23]:

$$\text{Oxidation (occurs at the anode):} \qquad \text{Cu}_{solid} \rightarrow \text{Cu}^{2+}_{aq} + 2e^-$$
$$\text{Reduction (occurs at the cathode):} \qquad \text{Cu}^{2+}_{aq} + 2e^- \rightarrow \text{Cu}_{solid}$$

where *aq* indicates that the copper is aqueous (dissolved in the solution), and *solid* indicates that the Cu is in a solid form (solidified on the anode or cathode). However, copper is not the only element that can be oxidized or reduced. In this design, the copper will exist in trace quantities within the zinc foil. Zinc could take the place of copper during reduction, thus electroplating zinc onto the metal cathode instead of radioactive copper. By changing the voltage and the pH of the acidic solution, the selectivity of copper can be adjusted [24]. For the electroplating method to succeed, the selectivity of copper must be high enough such

that the electroplated copper is $> 98\%$ pure [25]. In similar electroplating experiments, copper purity of approximately 90% has been obtained [24]. This purity is too low, and most experiments that have successfully separated copper from zinc using electroplating also used enriched Zn-64 [26]. However, in this design natural zinc is used. This will result in a wide range of impurities formed during zinc irradiation and will cause the final copper purity to decrease. For the case of Y-88 separation, there will be even greater difficulty since the $^{90}Zr(D, \alpha)^{88}Y$ has significantly more impurities formed during irradiation, as evidenced by the complexity of the zirconium foil gamma-ray spectra. For these reasons, electroplating was not chosen as the chemical separation method.

### 6.1.2. Ion Exchange Chromatography

Another chemical separation method is ion exchange chromatography. It is a process that allows ions to be separated based on their affinity for the ion exchange resin. There are two primary types of ion exchange chromatography for metal ions: cation exchange and anion exchange. Cation exchange allows for the separation of positively charged ions (*cations*) while anion exchange allows for the separation of negatively charged ions (*anions*).

As shown in the diagram below (Fig. 21), metal ions in a liquid solution can be poured onto a cation exchange resin. The resin is composed of millions of small, solid beads, typically 38 microns in diameter [27]. Each bead in a cation exchange resin is negatively charged but is coated with positively charged ions, typically $H^+$ [27]. As the $Cu^{2+}$ is exposed to the beads, the $H^+$ ions are forced off the solid bead and into the flowing liquid. This is called the transition from stationary phase to mobile phase. If negatively charged ions are present, they will be repelled by the negatively charged beads and thus remain in the liquid (mobile phase). Anion impurities, like $Cl^-$, are removed in the effluent stream. Once the anion impurities are removed, the $Cu^{2+}$ can be moved to the mobile phase by an increase in pH or salt concentration. Thus the final product is a purified $Cu^{2+}$ stream. If other cation impurities are present, such as $Zn^{2+}$, the pH or salt concentration can be adjusted very slowly. This allows for the $Cu^{2+}$ to elute before the $Zn^{2+}$.
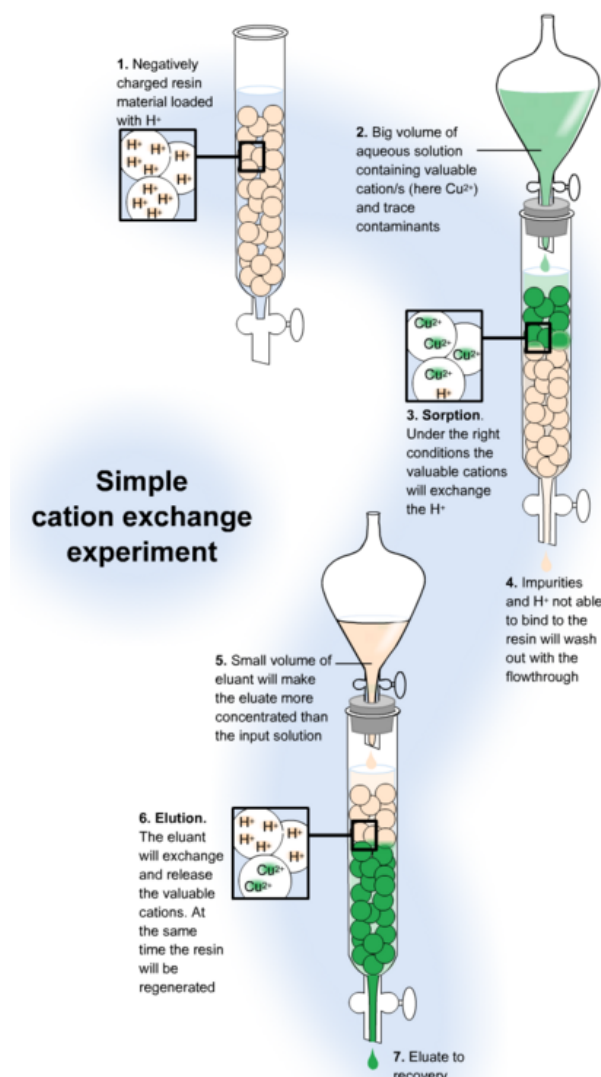
Figure 21: Diagram of a cation exchanger. It is composed of negatively charged resin beads coated with H$^+$ to maintain a net zero charge balance. Cu$^{2+}$ or another metal cation can be added and it will be retained in the resin. Negatively charged ions (anions) will pass through the resin and become eluted. Then the pH or salt content can be adjusted for the Cu$^{2+}$ to release from the resin beads and elute. *Figure adapted from Wikipedia* [? ].

Anion exchange works on the same principle but the charges are reversed. The solid resin bead is positively charged and is coated with anions, typically Cl$^-$[27]. Ion exchange columns are beneficial because they separate metals based upon affinity to the ion exchange resin (called *selectivity*). The selectivity of an ion is dependent upon its charge and its radius which is never identical for different ions. If two elements are similar in selectivity, the column length can be increased to improve separation. Thus copper and yttrium purities $> 98\%$ can be obtained which is a requirement for medical use of these radioisotopes. Furthermore, the yield is typically $> 90\%$ which means little of the copper and yttrium is discarded into the waste [26].

29

*6.2. Separation Design Choice*

As discussed previously, ion exchange chromatography is the preferred method to electroplating. It results in a higher purity, and is more robust when unexpected impurities are introduced. Moreover, it is a quick process so that substantial decay of the Cu-64 does not occur. A previous experiment has performed a similar copper-zinc separation using Dowex ion exchange resins, and a copper purity of nearly 100% was obtained which is very promising (the impurity concentration was so low it could not be detected) [26]. The design is similar to the cation exchange experiment described in Sec. 6.1.2. As shown in Fig. 22 below, this method uses two ion exchange columns.
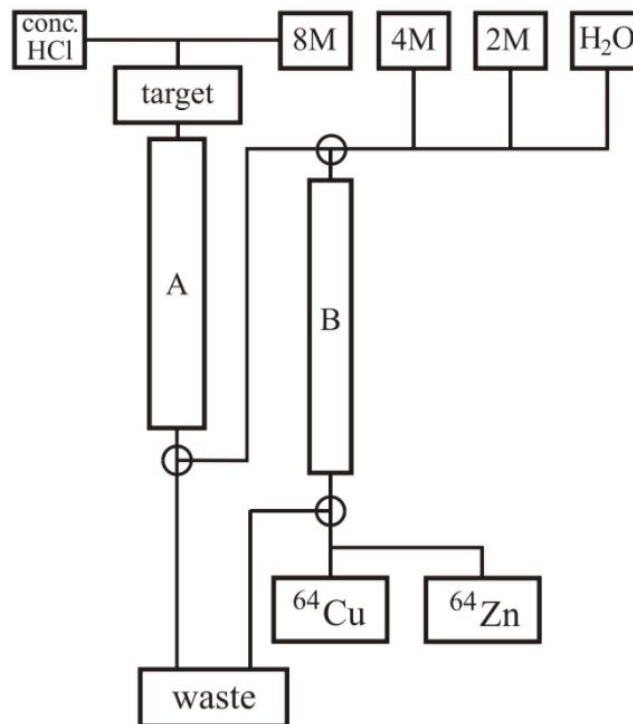


Figure 22: Diagram of dual column ion exchange method. The first column is a cation exchanger (labeled column A) where the anions and gallium are removed from the zinc and copper cations. The second column is an anion exchanger where the zinc and copper are separated. *Figure adapted from Kozempel, et. al.* [26].

First the zinc or zirconium foil is dissolved in concentrated ($> 8$ molar) HCl. For the zirconium foil, a slight amount of concentrated HF is added (typically a 10:1 HCl:HF molar ratio) to allow the zirconium to dissolve [26]. The first column is a cation exchanger composed of Dowex-50WX8-400. This resin is a strong base resin with negatively charged beads [27]. When the dissolved foil is introduced, negatively charged impurities, such as $Cl^-$ and $F^-$, will repel the negatively charged beads and pass through the column rapidly. For the first few minutes all liquid leaving the column will be sent to a waste beaker. Gallium ($Ga^{3+}$) impurities will stick to the resin beads and remain in the column. $Zn^{2+}$ and $Cu^{2+}$ will also stick to the beads, but with a lower selectivity. Thus they move through the resin slowly and are collected in a separate beaker once they reach the bottom of the column.

Next the $Cu^{2+}$ and $Zn^{2+}$ will be introduced to the top of the anion exchange column. This column is composed of Dowex-1X8-400 resin, which is a strong acid. The beads of this ion exchange resin are positively charged and they allow impurities such as $Na^+$ and $Co^{2+}$ to pass through the column quickly since they are repelled by the beads. Although $Zn^{2+}$ and $Cu^{2+}$ are positively charged and repel the beads, if the pH is kept low enough they will become fixed to the beads since they have a high selectively [? ]. As the pH is slowly increased, $Cu^{2+}$ will begin to preferentially elute. It can then be collected in a beaker and dried until only the solid Cu-64,67 is left. The pH can be further increased and the Zn can be collected in a separate beaker. This allows for the possibility of recycling the foil material. For example, the Zr-90 foil is extremely expensive due to its high enrichment. Thus recycling the Zr-90 after separating the Y-88 is possible and will greatly reduce the design costs.

Afterward, the columns can be "rinsed" with HCl to remove any impurities still inside the column. The waste can be collected in the same waste beaker as before. Disposal of the waste is discussed in the following section. After the cleaning step is performed, the columns are ready to be used again and a new Zn/Cu or Zr/Y foil separation can be performed.

## 6.3. Chemical, Radioactive, and Mixed Hazards

This portion of the design project is potentially the most hazardous. There are increased risks from handling of chemicals, radioactive material, and mixed radioactive/chemical material. These hazards must be properly managed and mitigated in any successful medical isotope production design. Chemical hazards include possible human exposure to strong acids (HCl, HF, Dowex-50WX8), strong bases (NaOH, Dowex-1X8), or toxins (F). Inhalation, ingestion, or even direct contact with any of these chemicals can cause serious injury. Lab technicians must wear close toed shoes, a spill resistant lab coat, long pants, goggles, and butyl rubber or neoprene rubber gloves (nitrile rubber, vinyl, and latex gloves will not prevent exposure to HF) [28]. Furthermore, they must be familiar with the Material Safety Data Sheet (MSDS) for each chemical contained in the lab. The lab must be an open, well ventilated space with quick access to an eye wash station, an emergency chemical shower, and a first aid kit containing calgonate gel (calgonate counteracts toxic effects of HF exposure) [28].

The radioactive hazards are potentially even more dangerous than the chemical hazards since they can not be easily spotted or detected. Thin foils of irradiated zinc and zirconium must be handled by lab technicians. If this material is vaporized during irradiation it could potentially be inhaled by lab workers. Full personal protective equipment must be worn, including radiation suits, masks, gloves, and protective glasses. For a commercialized process, it would be preferable to introduce as much automation as possible. Humans controlling robots from a distance greatly decreases the likelihood of radiation exposure. The ion exchange columns can also be fitted with pumps and a control system so that they are fully automatic, which will further reduce human exposure to radiation.

After elution, the final samples of copper and yttrium (as well as all waste material) will have its pH neutralized with NaOH. This eliminates most of the mixed waste present, and these samples can be treated as purely radioactive hazards. However, the ion exchange resins

will retain trace quantities of radioactive elements such as Y-88, Cu-64,67, Ga impurities, etc. If the chemical separation was performed on the University of California, Berkeley campus, the mixed waste could be stored for a maximum of 30 days and then must be shipped to Oak Ridge National Lab for disposal. Costs can run up to $4000 per liter of mixed waste [29]. However, if the separation is performed at Lawrence Berkeley National Lab (LBNL), the waste can be stored on site up to 1 year. After a year all of the radioactive impurities anticipated in this design will have decayed. Thus the ion exchange resins will become chemical waste and can be disposed of for less than $100 per liter [29]. Due to this substantial pricing difference, the chemical separation should be performed at a LBNL and all mixed and radioactive waste should be stored for 1 year to allow it to sufficiently decay. All disposal costs are estimated at < $100 per liter.

### 6.4. Design Costs

Table 9 below shows the unit cost and total cost of each item in the design project. The cost of all materials used in a single run is $65.82. The cost to run the accelerator for a single run is $2000 per hour [30]. The cost of disposal is >$100 per run. Thus the total cost is almost entirely dependent upon the accelerator time used. Current medical isotopes produced by accelerators often use a single foil or slab of material. A company or national lab could easily adapt a multistage foil design, such as this design, to increase their medical isotope production without a significant increase in production costs.

| Chemical | Hazards | Quantity | Unit Cost | Cost |
|---|---|---|---|---|
| HCl | Acidic | 20mL | $0.02/mL | $0.40 |
| HF | Acidic, toxic | 2mL | $0.11/mL | $0.22 |
| Dowex-50WX8-400 | Strong base | 50g | $0.55/g | $27.45 |
| Dowex-1X8-400 | Strong acid | 50g | $0.62/g | $30.95 |
| NaOH | Basic | 10g | $0.12/g | $1.20 |
| Zn (natural) | Radioactive after irradiation | 35g | $0.05/g | $1.86 |
| Zr-90 (enriched) | Radioactive after irradiation | 4mg | - | - |
| Al (natural) | None | 2kg | $1.87/kg | $3.74 |

Table 9: This table shows a summary of all the materials used in this design. It includes a brief overview of their hazards, the quantity required for a single separation to be performed, and the cost. The cost and hazard data was obtained from the chemical supply company Sigma Aldrich [27]. Enriched Zr-90 can be obtained for free from LBNL if it is returned after use for recycling [30].

## 7. Conclusions

A design for the simultaneous production of various medical isotopes using a single charged particle beam has been presented. A experimental test of this concept was performed and proved successful. Three medically relevant radioisotopes were produced: $^{90}Zr(D, \alpha)^{88}Y$, $^{64}Zn(n, p)^{64}Cu$, and $^{67}Zn(n, p)^{67}Cu$. An analytical model of the expected radioisotope yields was discussed. Further exploration of this model was performed using MCNP to predict

the spectra of key particles after each foil in the stack. A series of candidate materials were investigated through mechanical analysis and radiation studies for use in the deuteron breakup target, and ultimately an ideal material was selected. This material minimizes likelihood of plastic deformation and subsequent failure. A 3-D model of the proposed design was presented with the aid of SOLIDWORKS®. Heat transfer simulations using COMSOL Multiphysics® informed the safe operating bounds of the beam current and irradiation time. A chemical separation technique using dual ion exchange columns was selected that allows for quick, inexpensive, and high-purity separation of $^{64}$Cu, $^{67}$Cu, and $^{88}$Y.

### Acknowledgements

### References

[1] L. Bernstein, Simultaneous radionuclide production using (d,2n) and secondary neutron-induced (n,p) reactions, Tech. Rep. App. to DOE-FOA-0001588, UC Berkeley and Lawrence Berkeley National Laboratory (1 2014).

[2] M. R. Bhat, Evaluated Nuclear Structure Data File (ENSDF), Springer Berlin Heidelberg, Berlin, Heidelberg, 1992, pp. 817–821, data extracted using the NNDC On-Line Data Service from the ENSDF database, file revised as of (date). doi:10.1007/978-3-642-58113-7_227.
URL http://dx.doi.org/10.1007/978-3-642-58113-7_227

[3] J. D. B. K.M. Murdy, R. Plonsey, Biomedical Imaging, CRC Press, 2003, Ch. 14, p. 4.

[4] N. D. Community, Numpy license (2017).

[5] A. Koning, S. Hilarie, S. Goriely, Talys: A nuclear reaction program (12 2015).

[6] G. Knoll, Radiation Detection and Measurements, 4th Edition, John Wiley and Sons, 1981.

[7] J. Meulders, P. Leleux, P. Macq, C. Pirart, Fast neutron yields and spectra from targets of varying atomic number bombarded with deuterons from 16 to 50 mev, Phys. Med. Biol. 20 (2) (1975) 235–243.

[8] D. B. Pelowitz, Mcnpx user's manual, Tech. Rep. LA-CP-07-1473, Los Alamos National Laboratory (2008).

[9] S. Agostinelli, et al., GEANT4: A Simulation toolkit, Nucl. Instrum. Meth. A506 (2003) 250–303. doi:10.1016/S0168-9002(03)01368-8.

[10] J. Shackelford, Introduction to Materials Science for Engineers, 7th Edition, Prentice Hall, 2008.

[11] J. Ziegler, Srim - the stopping and range of ions in matter (2017).
URL http://www.srim.org/

[12] J. Ziegler, M. Ziegler, J. Biersack, SRIM The Stopping and Range of ions in Matter, 7th Edition, SRIM Co., Chester, Maryland, 2008.

[13] Zirconium, http://www.matweb.com/search/DataSheet.aspx?MatGUID=6e8936b3ad994f13bfb29923cc1506a9.

[14] Zinc, http://www.matweb.com/search/DataSheet.aspx?MatGUID=8909140a76074049809ad74d536ed606.

[15] Poisson's ratio of metals, http://www.engineeringtoolbox.com/metals-poissons-ratio-d_1268.html.

[16] J. Boylan, Carbon - graphite materials, http://www.azom.com/properties.aspx?ArticleID=516.

[17] Beryllium, http://www.matweb.com/search/DataSheet.aspx?MatGUID=8a6a0df6122349b7bdc92662658d4a4f.

[18] AZoM.com, Silicon carbide (sic) properties and applications, http://www.azom.com/article.aspx?ArticleID=42.

[19] Overview of materials for 6000 series aluminum alloy, http://www.matweb.com/search/DataSheet.aspx?MatGUID=26

[20] COMSOL Multiphysics® v. 5.2a., COMSOL AB, Stockholm, Sweden, www.comsol.com, 2016.

[21] L. A. Bernstein, D. Brown, A. Hurst, J. Kelly, F. Kondev, E. McCutchan, C. Nesaraja, R. Slaybaugh, A. Sonzongi, Nuclear data needs for capabilities and applications, Tech. Rep. LLNL-CONF-676585, Lawrence Livermore National Laboratory (05 2015).

[22] T. Henning, Wikipedia - electroplating, https://commons.wikimedia.org/wiki/File:Copper_electroplating.svg.

[23] D. Oxtoby, H. Gillis, A. Campion, Principles of Modern Chemistry, 7th Edition, Brooks/Cole, Belmont, California, 2008.

[24] J. L. L. Z. C. L. S. J. Taihong Shi, Shujian Zou, R. L. Qiu, Separation and recovery of nickel and copper from multi-metal electroplating sludge by co-extracting and selective stripping, Civil and Environmental Engineering 1 (1) (2011) 1–7. doi:10.4172/2165-784X.1000103.
URL http://www.omicsgroup.org/journals/separation-and-recovery-of-nickel-and-copper-from-multi-m 1000103.php?aid=3074

[25] C. . U. R. Inc., Us radiopharmaceuticals - copper-67, http://usradiopharma.us/products/copper-67/.

[26] F. S. e. a. J. Kozempel, K. Abbas, A novel method for n.c.a. 64cu production by the 64zn(d, 2p)64cu reaction and dual ion-exchange column chromatography, Radiochimica Acta 95 (2) (2009) 75–80. doi:10.1524/ract.2007.95.2.75.
URL    https://www.degruyter.com/view/j/ract.2007.95.issue-2/ract.2007.95.2.75/ract. 2007.95.2.75.xml

[27] Sigma-Aldrich, Sigma-aldrich product search, http://www.sigmaaldrich.com/catalog/product/sial/217514?lang=en&r

[28] H. U. D. of Chemistry, C. Biology, Guidelines for the safe use of hydrofluoric acid, https://chemistry.harvard.edu/files/chemistry/files/safe_use_of_hf_0.pdf.

[29] J. Corvino, J. Cromwell, Private Communication.

[30] E. Matthews, L. Bernstein, Private Communication.